

## Modeled precipitation variability over the Greenland ice sheet

David H. Bromwich,<sup>1</sup> Qui-shi Chen, Le-sheng Bai, Elizabeth N. Cassano,<sup>2</sup> and Yufang Li

Polar Meteorology Group, Byrd Polar Research Center  
Ohio State University, Columbus, Ohio, USA

**Abstract.** On the basis of the evaluation of recent Greenland precipitation studies, some of the deficiencies in the modeled precipitation are probably related to the topographic data employed in modeling. In this paper the modern digital elevation data of *Ekholm* [1996] is used. If the horizontal pressure gradient force in  $\sigma$  coordinates is separated into its irrotational and rotational parts, which are expressed by the equivalent geopotential and geo-stream-function, respectively, the topographic effect on the precipitation can be accurately modeled. The equivalent geopotential and geo-stream-function are implemented in a fully consistent manner in the generalized  $\omega$ -equation in this paper. A simplified large-scale condensation without evaporation of condensate is also used. These improvements are combined to yield an improved dynamic method. Two aspects of the precipitation distribution are refined by the improved dynamic method. One is the 10 cm yr<sup>-1</sup> contour near Summit, Greenland, and the other is a relative large precipitation area centered near the point (70°N, 49°W). Extensive comparisons are made between the retrieved precipitation and the observed annual accumulation time series from 11 ice core sites on the ice sheet. The modeled precipitation from the original method must use scalars to have a high degree of interannual correspondence between the measured accumulation and the retrieved precipitation, but the retrieved precipitation from the improved method increases at all ice core sites and a good correspondence is obtained without any scalar being required. The spatial average of multiyear mean error ( $\bar{\epsilon}_j$ ) is 11.5 cm yr<sup>-1</sup> for the modeled precipitation from the improved method, while that for  $P$  from ERA-15 is 14.5 cm yr<sup>-1</sup>. The total mean error ( $\epsilon_M$ ) is 3.0 cm yr<sup>-1</sup> for the improved method, while  $\epsilon_M$  for the  $P$  from ERA-15 is 4.0 cm yr<sup>-1</sup>. These two errors show that the precipitation modeled by the improved method is better than the  $P$  from ERA-15. Thus the distribution of precipitation over the 11 sites retrieved by the improved dynamic method is considerably refined. Large downward trends in annual amounts are present in the precipitation retrieved by the improved dynamic method for all of Greenland and its southern and central west coastal regions. The modeled precipitation from the improved dynamic method and observed accumulation from ice cores are all in agreement with the *Thomas et al.* [1999] result that the southern Greenland ice sheet above 2000 m is approximately in balance. It also shows that local thickening and thinning areas of the ice sheet derived by airborne laser altimetry from 1993 to 1999 over the entire Greenland above 2000 m [*Krabill et al.*, 2000] are approximately consistent with precipitation change retrieved by the improved dynamic method.

### 1. Introduction

To understand variations of accumulation over Greenland, it is necessary to investigate precipitation and its variations. Observations of precipitation over Greenland are limited and generally inaccurate, but the analyzed wind, geopotential height, and moisture fields are available for recent years. It is very useful to develop a dynamic method for retrieval of precipitation over Greenland from these analyzed fields.

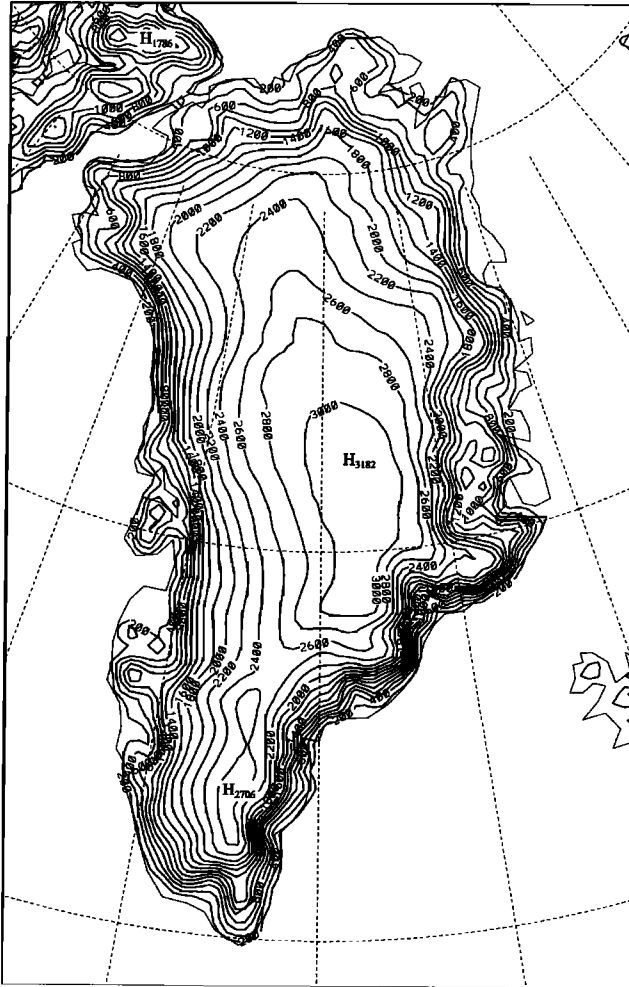
Precipitation over Greenland from 1985 to 1996 and their seasonal and interannual variations have been studied on the basis of the dynamic method, and the interannual variations have been related to those of the North Atlantic Oscillation (NAO) index [*Chen et al.*, 1997a; *Bromwich et al.*, 1999].

On the basis of the evaluation of recent Greenland precipitation studies [*Bromwich et al.*, 1993; *Kalnay et al.*, 1996; *Chen et al.*, 1997a; European Centre for Medium-Range Weather Forecasts (ECMWF) Reanalysis for 1979-1993 (ERA-15)], several of the deficiencies in the precipitation spatial distributions were investigated [*Bromwich et al.*, 1998]. One of the deficiencies is probably related to the topographic data employed in assimilation and modeling. The Matrikelstyrelsen and Ekholm [*Ekholm*, 1996] field is a realistic digital elevation data set synthesized from a variety of observations including satellite radar altimetry. Both the ERA-15 and the National Centers for Environmental Prediction (NCEP)/National Center for Atmospheric Research (NCAR)

<sup>1</sup>Also at Atmospheric Sciences Program, Department of Geography, The Ohio State University.

<sup>2</sup>Now at CIRES, University of Colorado, Boulder, Colorado.

(a) Old Terrain of Greenland



(b) New Terrain of Greenland

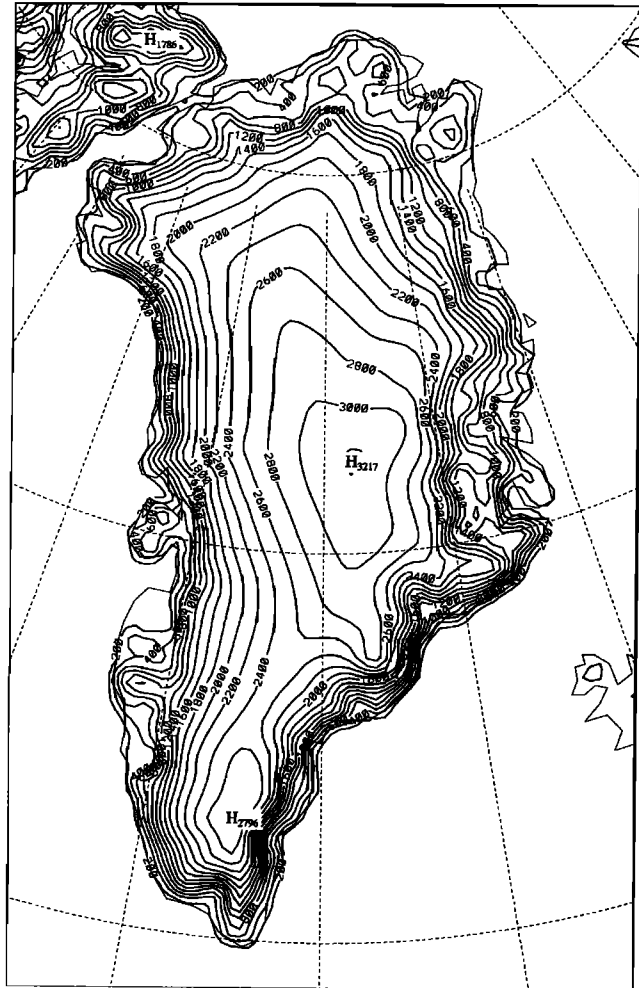


Figure 1. (a) Topography of Greenland and adjacent areas (in meters with a contour interval of 200 m) based on the U.S. Navy 10 arc min global data set; (b) same as Figure 1a but based on Ekholm [1996]. Notice the large difference over Greenland just to the south of 70°N.

reanalysis use the global U.S. Navy 10 arc min digital elevation data set. Chen *et al.* [1997a] and Bromwich *et al.* [1999] also elected to use this data set for their study. Genthon and Braun [1995] have identified substantial errors of up to 1 km in the U.S. Navy data set over the Antarctic ice sheet. The topography of Greenland from the U.S. Navy 10 arc minute global data set and the modern data set of Ekholm [1996] are shown in Figures 1a and 1b, respectively. The Navy depiction of the plateau region (for example, the 2800 and 3000 m contours) is found to extend too far to the south without a mesoscale ridge, and the major ridge (the 2600 m contour) in the southern region is too narrow. Such errors affect the calculated precipitation in these parts of Greenland. In this paper the topography of Greenland, shown in Figure 1b, is used in the simulation.

The topographic effects on precipitation and atmospheric motion are greatly influenced by the computational accuracy of the horizontal pressure gradient force over mountainous regions, especially near steep slopes of mountains and ice

sheets. Colle *et al.* [1999] verified the 36 and 12 km resolution Penn State/NCAR mesoscale model (MM5) precipitation forecasts and the NCEP 10 km resolution Eta model (Eta-10) forecasts across the Pacific Northwest of the United States and found that the 12 km MM5 tends to generate too much precipitation along the steep windward slopes. The Eta-10 overpredicts precipitation along the windward slopes even more than the 12 km MM5 although the step-mountain approach of the Eta-coordinate system is used. Recently, Cassano *et al.* [this issue] have used the MM5 to simulate a complete annual cycle from April 1997 to March 1998 over the Greenland ice sheet. The simulations are a series of 48 hour forecasts of which only the forecasts of the second 24 hour period are used to represent each day. The modeled precipitation distribution is excessive along the steep coastal margins with a value in excess of 400 cm yr<sup>-1</sup> located on the southeast coast, while the corresponding observed value is about 120 cm yr<sup>-1</sup>. The precipitation errors are similar to those over the Pacific Northwest found by Colle *et al.* [1999].

Recently, *Chen and Bromwich* [1999] (hereinafter referred to as CB99) showed that the horizontal pressure gradient force in  $\sigma$  coordinates can be computed more accurately by separating this horizontal vector into its irrotational and rotational parts, which are expressed by the equivalent geopotential and geo-stream-function, respectively.

The measured accumulation values from ice cores have many unique features. The timescale of the measured accumulation is comparatively long. For example, only annual values can usually be obtained, thus the timescale of significant temporal variability is several years. However, the horizontal scale of the measured accumulation is comparatively small. For example, the distance between some ice cores is about 10 km, yet the variations of the measured accumulation between these cores are often substantial due to spatial noise largely unrelated to snowfall differences. Thus the horizontal scale of accumulation variations is kilometers. For the annual timescale the day-to-day variations are unimportant. The generalized  $\omega$ -equation method studied by *Chen et al.* [1997a] is very useful for retrieving precipitation with low resolution in time but comparatively high resolution in horizontal space. This method can much more easily obtain a reasonable precipitation description over a long term than global and limited-area models. The equivalent geopotential has been partially used by *Chen et al.* [1997a] in their  $\omega$ -equation method. In section 2 a generalized  $\omega$ -equation in which the equivalent geopotential and geo-stream-function are implemented in a fully consistent manner is presented. The new enhanced method with the topography of Figure 1b in section 2 is referred to as the improved dynamic method.

A comparison of the annual mean precipitation over Greenland retrieved by the improved dynamic method from 1985 to 1999 to that computed from the original method and topography (Figure 1a) [*Chen et al.* 1997a] is presented in section 3, and some deficiencies of the retrieved precipitation are improved. Recently, measured annual values of net water equivalent accumulation from 11 ice core sites located near the 2000 m contour of the Greenland ice sheet were compared to the original retrieved precipitation [*Chen et al.* 1997a; *Bromwich et al.*, 1999] for 1985-1996 by *McConnell et al.* [2000a]. It was found that there is a high degree of correspondence in the interannual variations between the measured accumulation and the retrieved precipitation if scalars for the precipitation are used. In this paper, precipitation amounts over Greenland are retrieved again by the improved dynamic method, and the retrieved values are also compared with the measured time series of the accumulation rate from these ice cores. A good correspondence in the interannual variations between the measured accumulation and retrieved precipitation is obtained without the use of any scalars, and the results are also shown in section 3.

On the basis of the interannual precipitation variations produced by the improved dynamic method, the temporal variability of annual precipitation is evaluated in section 4. The relationship between the change of the surface elevation of the Greenland ice sheet observed by airborne laser altimetry and annual precipitation change retrieved from the improved dynamic method from 1993 to 1999 over Greenland above 2000 m is shown in section 4. The conclusions and some discussion are presented in section 5.

## 2. Generalized $\omega$ -Equation in $\sigma$ -Coordinates Based on the Equivalent Geopotential and Geo-Stream-Function, and an Improved Dynamic Method for Computing Precipitation

### 2.1. Equivalent Geopotential and Geo-Stream-Function in $\sigma$ -Coordinates

The horizontal wind can be separated into its irrotational and rotational parts and expressed by

$$\mathbf{V} = -\nabla\chi - \mathbf{k} \times \nabla\psi, \quad (1)$$

where  $\chi$  and  $\psi$  denote velocity potential and stream function, respectively.

The vertical coordinate  $\sigma$  is defined by  $\sigma = p/p_*$ , where  $p_*(x, y, t)$  is the surface pressure. The horizontal pressure gradient force  $\mathbf{G}$  in  $\sigma$  coordinates is expressed by

$$\mathbf{G} = -\nabla\phi(x, y, \sigma, t) - RT(x, y, \sigma, t)\nabla \ln p_*(x, y, t), \quad (2)$$

where  $\phi(x, y, \sigma, t)$  is the geopotential in  $\sigma$  coordinates. Here  $\mathbf{G}$  is also a horizontal vector. CB99 proposed that the vector  $\mathbf{G}$  can also be separated into its irrotational and rotational components and expressed by

$$\mathbf{G} = -\nabla\phi_e - \tilde{\mathbf{k}} \times \nabla\eta, \quad (3)$$

where  $\phi_e(x, y, \sigma, t)$  and  $\eta(x, y, \sigma, t)$  are referred to as an equivalent geopotential and a geo-stream-function, respectively.

The irrotational part  $-\nabla\phi_e(x, y, \sigma, t)$  must be equal to the irrotational part of the total vector on the right-hand side of (2). Thus we have

$$\begin{aligned} \nabla^2\phi_e(x, y, \sigma, t) = & \nabla^2\phi(x, y, \sigma, t) \\ & + \frac{\partial}{\partial x} \left\{ RT(x, y, \sigma, t) \frac{\partial \ln p_*}{\partial x} \right\} \\ & + \frac{\partial}{\partial y} \left\{ RT(x, y, \sigma, t) \frac{\partial \ln p_*}{\partial y} \right\}. \end{aligned} \quad (4)$$

If equation (4) is solved in a limited region, the geopotential and equivalent geopotential in  $\sigma$  coordinates can be separated into its inner and harmonic parts [*Chen and Kuo*, 1992] as

$$\begin{aligned} \phi &= \phi_i(x, y, \sigma, t) + \phi_h(x, y, \sigma, t), \\ \phi_e &= \phi_{ei}(x, y, \sigma, t) + \phi_{eh}(x, y, \sigma, t). \end{aligned} \quad (5)$$

On the basis of (4), the inner part of the equivalent isobaric geopotential height in  $\sigma$  coordinates,  $\phi_{ei}$ , can be derived from the solution of the following Poisson equation:

$$\nabla^2\phi_{ei} = \nabla^2\phi_i + \frac{\partial}{\partial x} \left( RT \frac{\partial \ln p_*}{\partial x} \right) + \frac{\partial}{\partial y} \left( RT \frac{\partial \ln p_*}{\partial y} \right), \quad (6)$$

with zero Dirichlet boundary value.

Because the horizontal pressure gradient force  $-\nabla\phi(x, y, p, t)$  in  $p$ -coordinates is also irrotational, the equivalent geopotential  $\phi_e(x, y, \sigma, t)$  can be used in  $\sigma$  coordinates in the same way as  $\phi(x, y, p, t)$  is used in  $p$ -coordinates. In the present paper, 16  $\sigma$ -levels at  $\sigma=0.025$ ,

0.075, 0.125, 0.170, 0.240, 0.325, 0.430, 0.550, 0.610, 0.670, 0.775, 0.855, 0.915, 0.955, 0.980, and 0.995 are used in the vertical. The equivalent geopotential  $\phi_e$  can be used on constant  $\sigma$  surface to improve synoptic analysis over high mountain regions [Chen and Bromwich, 1999]. Because of pressure reduction to sea level, some artificial small but strong high-pressure systems in the sea level pressure (SLP) analysis often occur over Greenland. These artificial systems can be removed by equivalent geopotential analysis on the constant  $\sigma$  surface at  $\sigma=0.995$ .

The inner part of the equivalent isobaric geopotential can be separated into geostrophic and ageostrophic parts. The geostrophic part is expressed by  $\phi_{e,ig} = f_0\psi_i$ , while the ageostrophic part is denoted by

$$\phi_{e,ia} = \phi_{ei} - \phi_{e,ig} = \phi_{ei} - f_0\psi_i, \quad (7)$$

where the Coriolis parameter is separated into

$$f = f_0 + f'. \quad (8)$$

Here  $f_0$  is the average value in the integration region, and  $f'$  is its deviation. If the atmospheric motion is quasi-geostrophic, the ageostrophic geopotential always vanishes. It is found in observational analyses near and over high-mountain regions that the geostrophic approximation ( $\phi_{ei} = f_0\psi_i$ ) between the equivalent geopotential and the stream function for synoptic scale motions is approximately satisfied directly on the constant  $\sigma$ -surfaces.

## 2.2. Vorticity and Divergence Equations in $\sigma$ Coordinates

The vorticity and divergence equations can be transformed into the equations of the inner parts of the stream function and velocity potential, respectively, and based on equations (5.17) and (5.18) of CB99, they are expressed by

$$\frac{\partial \psi_i \downarrow}{\partial t} + f_0 \chi_i \downarrow = \psi_{adv,i} \downarrow, \quad (9)$$

$$\frac{\partial \chi_i \downarrow}{\partial t} + \phi_{e,ia} \downarrow = \chi_{adv,i} \downarrow - E_i \downarrow \quad (10)$$

where the column vector  $X \downarrow$  of a variable  $X$  is denoted by

$$X \downarrow = (X_1, \dots, X_k, \dots, X_N)^T, \quad (11)$$

and  $(\dots)^T$ , is for transpose, and  $N$  is the total number of  $\sigma$ -levels. Here the term  $E_i \downarrow$ , is denoted by  $E_i \downarrow = [m^2(U^2 + V^2)]/2 \downarrow$ , and the terms  $\psi_{adv,i} \downarrow$  and  $\chi_{adv,i} \downarrow$  are the variation rates of the inner parts of the stream function and velocity potential caused by advection, respectively.

## 2.3. Vertical Finite Difference Forms of the Continuity, Hydrostatic and Thermodynamic Equations

To develop the equivalent geopotential equation, the vertical finite difference forms of the continuity, hydrostatic, and thermodynamic equations need to be used. On the basis of equation (6.1) of CB99, the vertical finite difference form of the continuity equation is written as

$$\frac{\partial \ln p_*}{\partial t} + m_0^2 \Pi D \downarrow = P_{adv}, \quad (12)$$

where  $D \downarrow$  is the column vector of horizontal divergence and  $\Pi$  indicates the row vector as

$$\Pi = (\Delta\sigma_1, \dots, \Delta\sigma_k, \dots, \Delta\sigma_N), \quad (13)$$

Similar to (8), the map scale factor is separated by  $m^2 = (m^2)_0 + (m^2)'$ , and  $(m^2)_0$  and  $(m^2)'$  are the average value in the integration region and deviation, respectively, and the term  $P_{adv}$  is dominated by the surface pressure advection and it is expressed by

$$P_{adv} = -m^2 \sum_{j=1}^N \left( U_j \frac{\partial \ln p_*}{\partial x} + V_j \frac{\partial \ln p_*}{\partial y} \right) \Delta\sigma - (m^2)' \Pi D \downarrow. \quad (14)$$

The inner part of equation (12) is written as

$$\frac{\partial \ln p_{*i}}{\partial t} + m_0^2 \Pi \nabla^2 \chi_i \downarrow = P_{adv,i} + m_0^2 \Pi \nabla^2 \chi_{hi} \downarrow, \quad (15)$$

where

$$D = D_i + D_h, \quad D_i = \nabla^2 \chi_{ii}, \quad D_h = \nabla^2 \chi_{hi}, \\ \nabla^2 \chi_i \downarrow = \nabla^2 \chi_{ii} \downarrow + \nabla^2 \chi_{hi} \downarrow. \quad (16)$$

The finite difference form of the hydrostatic equation based on (6.7) of CB99 is expressed by

$$\phi \downarrow = \phi_* \downarrow + RBT \downarrow, \quad (17)$$

where matrix  $B$  is an upper triangular matrix shown by equation (A.29) of Chen *et al.* [1997b], and  $\phi_* \downarrow = \phi_* I$ . Here  $I$  is the identity matrix and  $\phi_* \downarrow = \phi_* H_*$ , where  $H_*$  is the height of the Earth's surface.

The temperature can be separated into two parts:

$$T(x, y, \sigma, t) = T_0(\sigma) + T'(x, y, \sigma, t) \\ = T_0(\sigma) + (T(x, y, \sigma, t) - T_0(\sigma)), \quad (18)$$

where  $T_0(\sigma)$  is the averaged value of  $T(x, y, \sigma, t)$  over the constant  $\sigma$ -surface, and  $T'$  is its deviation. The temperature separation (18) is different from that of (5.2) and (6.9) of CB99 but is the same as that used by Chen *et al.* [1997b]. The separation (18) is more natural than separation (5.2) and (6.9) used by CB99. Based on (2.28) of Chen *et al.* [1997b], the vertical difference form of the thermodynamic equation is written as

$$\frac{\partial T \downarrow}{\partial t} = T_{had} \downarrow - m_0^2 F D \downarrow, \quad (19)$$

where

$$T_{had} \downarrow = T_{adv} \downarrow - (m^2)' F D \downarrow + P_T \downarrow. \quad (20)$$

Here the matrix  $F$  is denoted by equation (A.34) of Chen *et al.* [1997b], and  $P_T$  is the diabatic heating. The inner part of the thermodynamic equation is denoted by

$$\frac{\partial T_i \downarrow}{\partial t} = T_{had,i} \downarrow - m_0^2 F \nabla^2 \chi_i \downarrow + m_0^2 F \nabla^2 \chi_{hi} \downarrow. \quad (21)$$

## 2.4. The Equations of the Equivalent Geopotential and Ageostrophic Geopotential

Substituting the inner part of the hydrostatic equation (17) into (6), the vertical difference form of (6) is expressed by

$$\begin{aligned} \phi_{ei} \downarrow = & \phi_{*i} \downarrow + RBT_i \downarrow \\ & + \nabla^{-2} \left[ \frac{\partial}{\partial x} \left( RT \downarrow \frac{\partial \ln p_*}{\partial x} \right) + \frac{\partial}{\partial y} \left( RT \downarrow \frac{\partial \ln p_*}{\partial y} \right) \right], \end{aligned} \quad (22)$$

where  $\phi_{*i}$  is the inner part of  $\phi_*$ . Taking the partial derivative of (22) with respect to  $t$ , and utilizing (18), we have

$$\begin{aligned} \frac{\partial \phi_{ei} \downarrow}{\partial t} = & RB \frac{\partial T_i \downarrow}{\partial t} + RT_0 \downarrow \frac{\partial \ln p_*}{\partial t} \\ & + \nabla^{-2} \left[ \frac{\partial}{\partial x} \left( RT' \downarrow \frac{\partial \ln p_*}{\partial x} \right) + \frac{\partial}{\partial y} \left( RT' \downarrow \frac{\partial \ln p_*}{\partial y} \right) \right] \\ & + \nabla^{-2} \left[ \frac{\partial}{\partial x} \left( R \frac{\partial T \downarrow}{\partial t} \frac{\partial \ln p_*}{\partial x} \right) + \frac{\partial}{\partial y} \left( R \frac{\partial T \downarrow}{\partial t} \frac{\partial \ln p_*}{\partial y} \right) \right], \end{aligned} \quad (23)$$

where there are two more additional terms on the right-hand side of (23) than on that of (6.16) in CB99. Substituting (12), (15), (19), and (21) into (23), then (23) becomes

$$\frac{\partial \phi_{ei} \downarrow}{\partial t} + m_0^2 A \nabla^2 \chi_i \downarrow = \Phi_{e,had,i} \downarrow + m_0^2 A \nabla^2 \chi_{hi} \downarrow, \quad (24)$$

where matrix  $A$  is

$$A = R(BF + T_0 \downarrow \Pi), \quad (25)$$

and  $\Phi_{e,had,i} \downarrow$  denotes the variation rate of the inner part of the equivalent geopotential caused by the advection and heating and it is expressed by

$$\begin{aligned} \Phi_{e,had,i} \downarrow = & RBT_{had,i} \downarrow + RT_0 \downarrow P_{adv,i} \\ & + \nabla^{-2} R \left[ \frac{\partial}{\partial x} \left( T' \downarrow \frac{\partial (P_{adv} - m_0^2 \Pi D \downarrow)}{\partial x} \right) + \frac{\partial}{\partial y} \left( T' \downarrow \frac{\partial (P_{adv} - m_0^2 \Pi D \downarrow)}{\partial y} \right) \right] \\ & + \nabla^{-2} R \left[ \frac{\partial}{\partial x} \left( T_{had} \downarrow - m_0^2 FD \downarrow \right) \frac{\partial \ln p_*}{\partial x} \right] + \frac{\partial}{\partial y} \left[ \left( T_{had} \downarrow - m_0^2 FD \downarrow \right) \frac{\partial \ln p_*}{\partial y} \right] \end{aligned} \quad (26)$$

Here there are also two more additional terms on the right-hand side of (26) than on that of (6.19) in CB99. With these two additional terms, the variation rate of the inner part of the equivalent geopotential caused by the advection and heating,  $\Phi_{e,had,i} \downarrow$ , can be described more accurately.

On the basis of (7), the equation of the ageostrophic geopotential can be derived from (9) and (24) and expressed by

$$\frac{\partial \phi_{e,ii} \downarrow}{\partial t} + m_0^2 A \nabla^2 \chi_i \downarrow - f_0^2 \chi_i \downarrow = \Phi_{e,had,ii} \downarrow + m_0^2 A \nabla^2 \chi_{hi} \downarrow, \quad (27)$$

where

$$\Phi_{e,had,ii} \downarrow = \Phi_{e,had,i} \downarrow - f_0 \Psi_{adv,i}, \quad (28)$$

is referred to as the variation rate of the ageostrophic geopotential caused by advection and diabatic heating.

## 2.5. Generalized $\omega$ -Equation in $\sigma$ -Coordinates

If the tendencies of the velocity potential and ageostrophic geopotential in (10) and (27) are neglected, this approximation is referred to as a balanced ageostrophic approximation [Chen *et al.* 1996]. Thus equation (27) becomes

$$m_0^2 A \nabla^2 \chi_i \downarrow - f_0^2 \chi_i \downarrow = \Phi_{e,had,ii} \downarrow + m_0^2 A \nabla^2 \chi_{hi} \downarrow. \quad (29)$$

Equation (29) is a velocity potential form of the generalized  $\omega$ -equation for the balanced ageostrophic approximation in  $\sigma$  coordinates. In this equation the diabatic and advection terms computed by the ageostrophic wind are the same as those in the generalized  $\omega$ -equation in  $p$ -coordinates [Pauley and Nieman, 1992], but the effect of orography on the vertical

motion is much better described than that in  $p$ -coordinates. In the balanced ageostrophic approximation the rotational and divergent components of the ageostrophic wind are much more accurate than those in the quasi-geostrophic approximation, but the propagation of gravity waves is ignored, which may affect some mesoscale features of the retrieved precipitation. To reduce computational errors in the solution of (29), a harmonic-sine spectral method [Chen and Kuo, 1992] is used. If equation (29) is transformed into  $p$ -coordinates, and the term  $\Phi_{e,had,ii} \downarrow$  is computed by the geostrophic wind and expressed by  $\Phi_{e,had,ii,s} \downarrow$ , equation (29) can be reduced to a velocity potential form of the quasi-geostrophic  $\omega$ -equation.

From the solution  $\chi_i$  of (29), the divergence is computed by  $D = \nabla^2 \chi_i$ . Using the continuity equation and vertical finite differencing, the pressure vertical velocity in  $\sigma$  coordinates,  $\omega$  is expressed by

$$\left( \frac{\omega}{p} \right) \downarrow = m^2 (I - C) \left( U \downarrow \frac{\partial \ln p_*}{\partial x} + V \downarrow \frac{\partial \ln p_*}{\partial y} \right) - m^2 CD \downarrow, \quad (30)$$

where  $c$  is a lower-triangular matrix and shown by (A.15) of Chen *et al.* [1997b].

## 2.6. Simple Method for Computing Precipitation

The procedure for computing precipitation from the vertical motion is presented by Chen *et al.* [1997a], and only large-scale condensation is considered. In this paper the large-scale condensation is further simplified. Condensation from the saturated air is denoted by  $dq_s/dt$ , where  $q_s$  is the saturation-specific humidity. The moisture conservation equation, which allows for condensation, is expressed by

$$\frac{\partial q}{\partial t} = -\vec{v} \cdot \nabla q - \omega \frac{\partial q}{\partial p} - \frac{dq_s}{dt} + \frac{S_j}{\rho}, \quad (31)$$

where  $q$  is specific humidity and  $S_j/\rho$  represents possible sources or sink of moisture other than condensation. Assuming no other heat sources, condensation takes place as a result of saturated adiabatic expansion, and the condensate precipitates. On the basis of Haltiner and Williams [1980, p. 309], the condensation rate can be expressed by

$$\frac{dq_s}{dt} = \delta F \omega, \quad (32)$$

where the condensation function  $F$  is denoted by

$$F = \frac{q_s T}{p} \left( \frac{LR - C_p R_v T}{C_p R_v T^2 + q_s L^2} \right). \quad (33)$$

Here  $L$  is the latent heat of condensation, and  $R_v$  is the gas constant for moist air. The Kronecker delta  $\delta$  is denoted by

$$\delta = 1: \text{ for } \omega < 0 \text{ and } r \geq r_c, \quad \delta = 0: \text{ for } \omega \geq 0 \text{ and } r < r_c, \quad (34)$$

Here the condensation may be assumed to begin at some critical relative humidity  $r_c$  less than 100%. In this paper the critical relative humidity  $r_c$  is assumed to be 83% based on computed precipitation experiments.

If all of the condensate from the saturated expansion is assumed to fall instantly as precipitation, the precipitation  $P$  per unit area in a time period  $\Delta t$  becomes

$$P = \int_t^{t+\Delta t} \int_{z_c}^{\infty} -\frac{dq_s}{dt} \rho dz dt = - \int_t^{t+\Delta t} \int_{z_c}^{\infty} \frac{P_*}{g} \delta F \omega d\sigma dt, \quad (35)$$

where  $Z_s$  is height of the earth's surface. The precipitation is calculated twice per day based on the operational analyses at 0000 and 1200 UTC from ECMWF. Each of the precipitation computation is for a time period  $\Delta t$  of 12 hours. The annual precipitation is derived by adding daily precipitation amounts for the whole year.

In the condensation scheme of *Chen et al.* [1997a] the condensed excess water removed from an atmospheric layer precipitates into the layer immediately below. The falling precipitation either evaporates completely in that layer or brings the layer to saturation and then the excess water passes to the next layer below again. The process is repeated. Only when the lowermost layer is saturated, does the condensed water precipitate onto the ground as snow or rain. Thus this condensation scheme includes not only condensation but also evaporation. However, this evaporation is not the same as the evaporation that takes place in the real atmosphere. In the simplified condensation scheme of the present paper, all of the condensate from the saturated expansion is assumed to fall instantly as precipitation.

There are three differences between the dynamic method used by *Chen et al.* [1997a], CB99 and *Bromwich et al.* [1999] and that used in the present paper. The first is that the equivalent geopotential and geo-stream-function are implemented in a fully consistent manner in this paper, with the term  $\phi_{e,hud,i} \downarrow$  in the generalized  $\omega$ -equation being expressed by (26) instead of (6.19) of CB99. The second is that the corrected topography of Figure 1b is used, and the third is that the large-scale condensation scheme is further simplified without any evaporation of condensate. The new enhanced dynamic method is referred to as the improved dynamic method in this paper.

### 3. Annual Mean Precipitation Over Greenland From 1985 to 1999 Retrieved by the Improved Dynamic Method and Its Comparison with Measured Accumulation From Ice Cores

#### 3.1. Annual Mean Precipitation Over Greenland From 1985-1999 Retrieved by the Improved Dynamic Method

To check how the computed precipitation is affected by the improved dynamic method, the distribution of the mean annual precipitation for 1985-1999 is shown in Figure 2b, while that for 1985-1995 computed from the original method [*Chen et al.*, 1997a] based on the topography of Figure 1a is shown in Figure 2a. Figure 2c shows Csatho-PARCA (Program for Arctic Regional Climate Assessment) accumulation map [*Csatho et al.*, 1997] based on a recent reexamination of the available data, and it may have errors in marginal areas of the ice sheet. The accumulation is a net result of precipitation, evaporation/sublimation and drifting. However, only precipitation is calculated in this paper, and it closely approximates accumulation over the ice sheet interior. Comparing Figures 2a and 2b with 2c, the precipitation amount computed from the improved dynamic method in the central region near Summit (72.3°N, 35.9°W) increases. The area of the 10 cm yr<sup>-1</sup> contour in Figure 2b is smaller than the northern feature in Figure 2a, and there is no second closed 10 cm yr<sup>-1</sup> contour in Figure 2b, as there is in Figure 2a near Summit. Thus the distribution of the 10 cm yr<sup>-1</sup> contour in Figure 2b is much closer to the measured accumulation of

Figure 2c than that in Figure 2a. Notice that there is a temporal discrepancy between the long-term average accumulation (Figure 2c) and the precipitation calculation for recent years (Figures 2a and 2b).

To demonstrate the better performance of the improved method over the old one, a difference map (Figure 2b minus Figure 2a) is shown in Figure 2d. In general, precipitation in Figure 2d is positive except for some small negative areas along the coast. It is seen from the heavy zero isoline in Figure 2d that there are two negative areas along the southeast coast and two small negative areas along the southwest coast; small negative differences are found along the north coast.

It is mentioned in section 1 that a comparison between the measured accumulation from 11 ice core sites located near the 2000 m contour of the Greenland ice sheet and the precipitation computed from the original method was studied by *McConnell et al.* [2000a] and a high degree of correspondence between them can be found if scalars are used for the precipitation. Figure 2d also shows that the precipitation retrieved by the improved method along the 2000 m contour is roughly 20 to 30 cm yr<sup>-1</sup> larger than the precipitation shown in Figure 2a (without scalars) retrieved by the original method.

In Figure 2c, there is a relative large accumulation with the contour value of 50 cm yr<sup>-1</sup> in the region centered near the point (70°N, 47°W), but there is no corresponding large precipitation center in Figure 2a in this region. However, a relatively large precipitation area and a positive center are located near the point about (70°N, 47°W) in Figures 2b and 2d, respectively. Thus the computed precipitation in this region is better in Figure 2b than in Figure 2a, although the location of the center is a couple of degrees of longitude to the west of that of the accumulation feature in Figure 2c. In the improved dynamic method, the lateral boundary condition is better resolved.

The accumulation of Figure 2c has many mesoscale features, which may be affected by the mesoscale characteristics of topography in this region. The data sets (TOGA Archive from NCAR or ERA data) of the analyzed wind, geopotential height, and moisture fields used in this study are large scale with 2.5°x2.5° resolution. These data sets must reflect the resolution (2.5°x2.5°) of the topography adopted at the forecast center (here ECMWF) from which the analyses originate. This may have an impact on the precipitation results, and it may be closely related to the relatively large precipitation area along the western slopes of the southern part of the Greenland ice sheet. This shows that the mesoscale features of the annual mean precipitation over Greenland need further improvement, especially over southern Greenland. The problem of how to use the large-scale 2.5°x2.5° resolution analyzed data and mesoscale high-resolution topography to obtain a mesoscale high-resolution precipitation distribution over Greenland needs further investigation.

*Anthes* [1990] showed that a mesoscale model with realistic treatment of mesoscale topography, Earth surface conditions, and physical processes is capable of developing mesoscale phenomena and precipitation from good large-scale initial conditions. Physically, this means that a mesoscale model can produce mesoscale systems after a certain time integration through interactions and feedbacks between the large-scale initial conditions and the mesoscale topography, Earth surface conditions, and physical processes. The

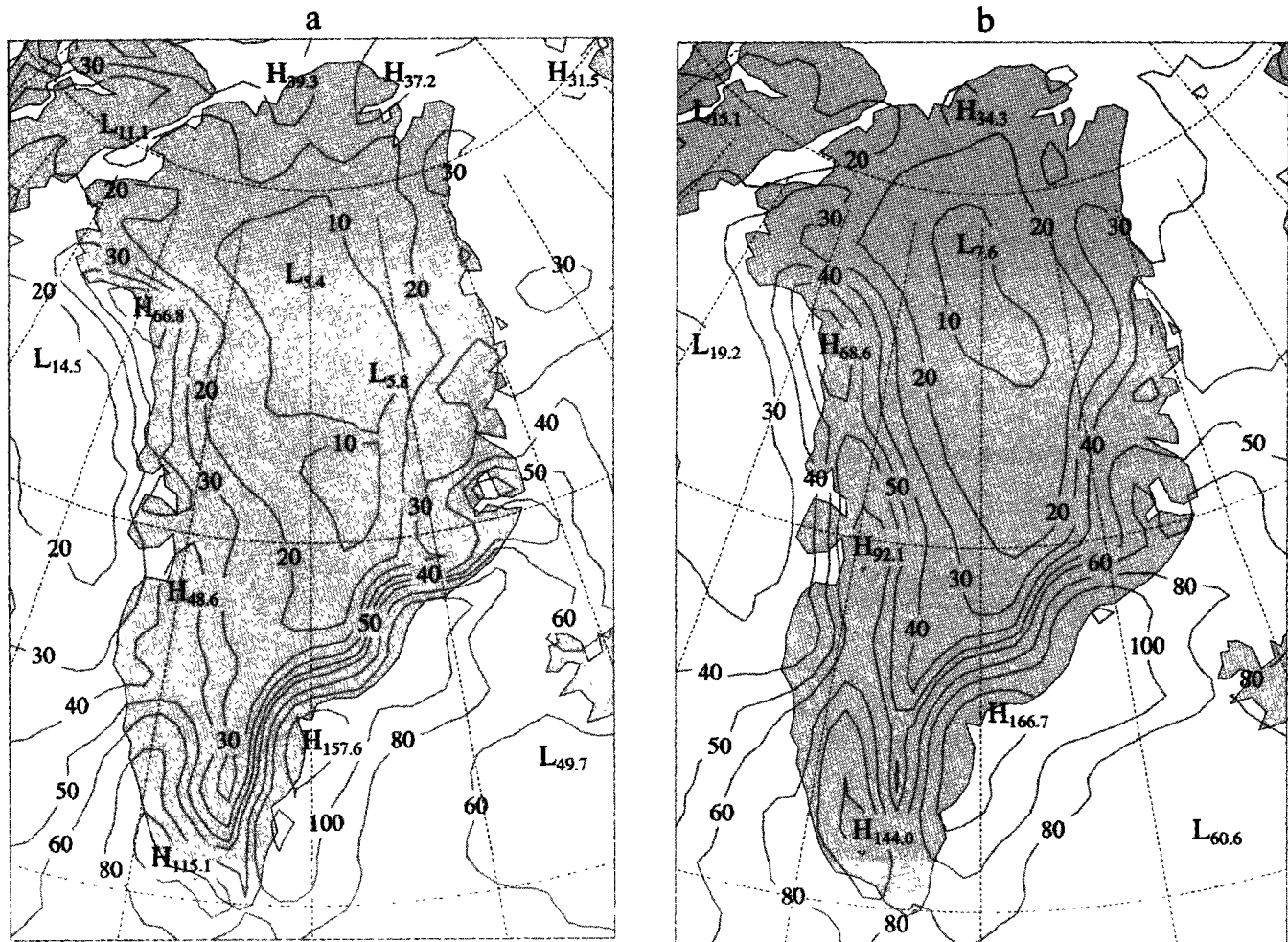


Figure 2. (a) Mean annual precipitation for 1985-1995 retrieved by the original method with the topography of Figure 1a in centimeters with a contour interval of 20 cm, but 10 cm if smaller than 40, and 30 cm if larger than 100; (b) same as Figure 2a but for 1985-1999 retrieved by the improved method based on the topography of Figure 1b; (c) Csatho-PARCA accumulation distribution of Greenland [Csatho *et al.*, 1997]. Observational data points are indicated as small stars. Large stars indicate coastal gauge stations. Recently, available accumulation data points are indicated as solid diamonds. The contour interval is 5 cm yr<sup>-1</sup> water equivalent for values less than 30 cm yr<sup>-1</sup> and 10 cm yr<sup>-1</sup> for values greater than 30 cm yr<sup>-1</sup>. (d) The computed precipitation difference between the improved dynamic method and the old one (improved - old). The contour interval is 10 cm yr<sup>-1</sup>.

generalized  $\omega$ -equation is a diagnostic relation; it derives precipitation immediately and does not include enough interactions and feedbacks between the large-scale initial conditions and mesoscale topography even if the mesoscale topography is correctly specified. Thus it is difficult to generate correct mesoscale systems from the large-scale initial conditions. This is an important weakness of the improved dynamic method in comparison to mesoscale models. In the near future, we plan to use a dynamic initialization method to adjust the large-scale ( $2.5^\circ \times 2.5^\circ$ ) resolution analyzed data to be consistent with the mesoscale high-resolution topography and then use the initialized data in the generalized  $\omega$ -equation to improve the simulation of mesoscale features of Greenland precipitation.

### 3.2. Comparison of Interannual Variations at Ice Core Sites in Greenland Between Measured Accumulation and Modeled Precipitation

The locations of the 11 ice core sites near the 2000 m contour of the Greenland Ice Sheet studied by McConnell *et al.* [2000a] are shown in Figure 3. The annual variations of the recently measured time series of net water equivalent accumulation from these 11 ice core sites are shown in Figures 4a-4d, respectively.

The precipitation amounts at the grid points retrieved from dynamic methods are interpolated to the ice core locations. The interannual variations of the precipitation at the ice core sites retrieved from the improved dynamic method for 1985-

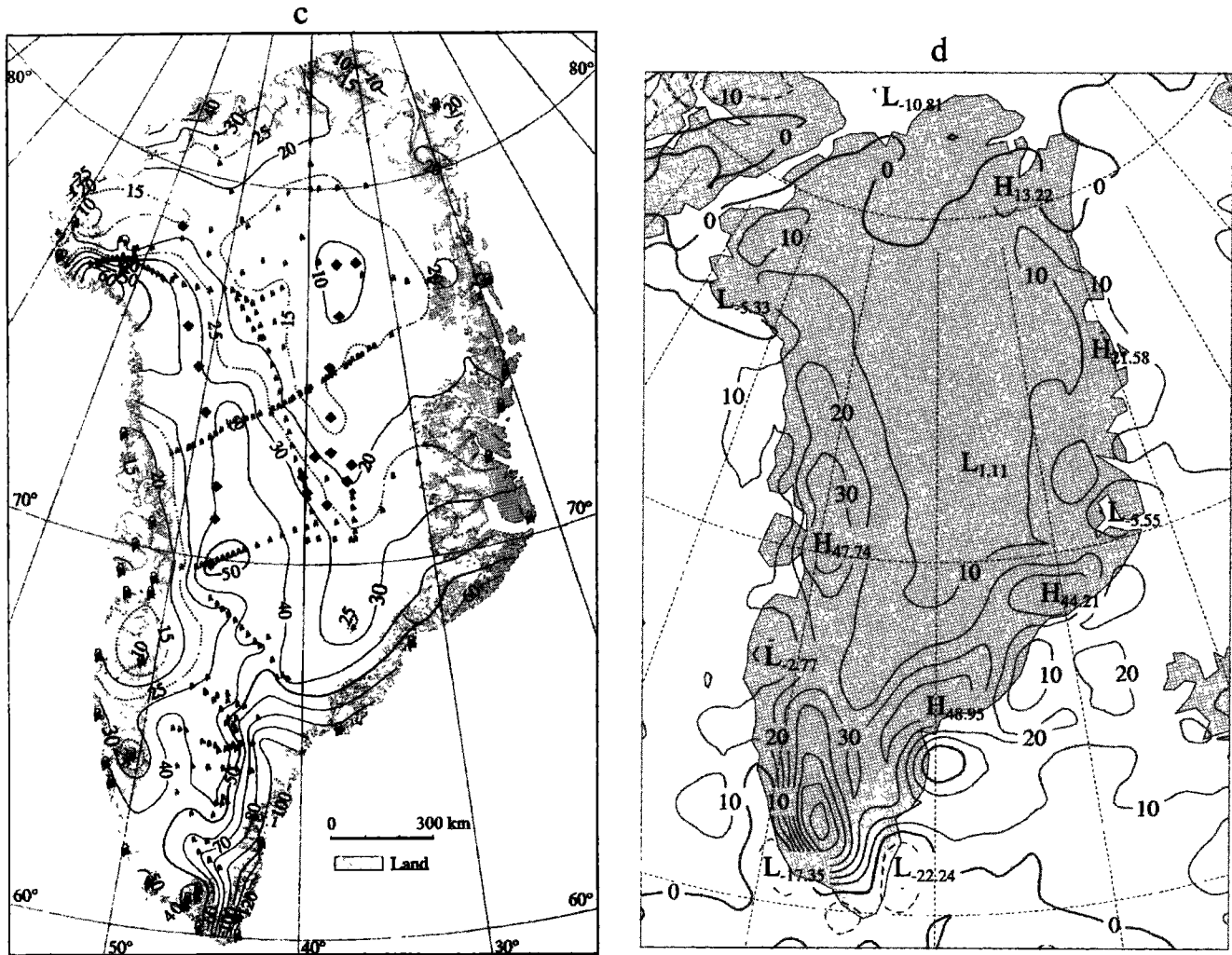


Figure 2. (continued)

1999 and those computed from the original dynamic method of *Chen et al.* [1997a], based on the topography of Figure 1a, for 1985-1997 are also shown in these figures; the scalars used by *McConnell et al.* [2000a] for the original method have been removed. It is seen from Figures 4a-4d that the values of the retrieved precipitation from the method of *Chen et al.* [1997a] based on the topography of Figure 1a for 1985-1995 at all sites are lower than those of the measured accumulation. *McConnell et al.* [2000a] showed that this modeled precipitation must use scalars to yield a high degree of correspondence in the interannual variations between the measured accumulation and retrieved precipitation. However, if the improved dynamic method is used, the retrieved precipitation increases at these ice cores, and a good correspondence in the interannual variations between the measured accumulation and the retrieved precipitation is obtained without any scalars being required.

ERA-15 [*Gibson et al.*, 1997] is a 15-year data assimilation product for the period 1979-1993, and it provides the values of precipitation  $P$  and the difference between the precipitation and the evaporation/sublimation,  $P - E$ . *Bromwich et al.* [1998] found that the Greenland precipitation estimates from the original dynamic method and ERA-15 were similar, and E.

Hanna (personal communication, 2000) has recently emphasized the comparatively high performance of the ERA-15 predicted precipitation amounts in Greenland, so the comparison of precipitation amounts retrieved from the improved dynamic method with those based on ERA-15 is continued here. The interannual variations of the values of  $P$  and  $P - E$  from ERA-15 data at the ice core sites are shown in Figures 4a-4d. Because we only have the ERA-15 data for 1979-1993 and ECMWF operational data from TOGA Archive II from NCAR for 1985-1999, a common 9 year period 1985-1993 is chosen for comparison. For this purpose, the multiyear mean error at site  $j$  over the 9 years  $\varepsilon_j$  of the modeled annual precipitation is defined by

$$\varepsilon_j = \frac{1}{Y} \sqrt{\sum_{y=1}^Y ((mod)_{j,y} - (obs)_{j,y})^2}, \quad (36)$$

where  $(obs)_{j,y}$  and  $(mod)_{j,y}$  denote the observed annual accumulation and modeled annual precipitation for year  $y$  at site  $j$ , respectively. The multiyear mean error at site  $j$  describes the mean difference between the two interannual variation curves of the observed accumulation and modeled precipitation over the 9 years at this site. The spatial average

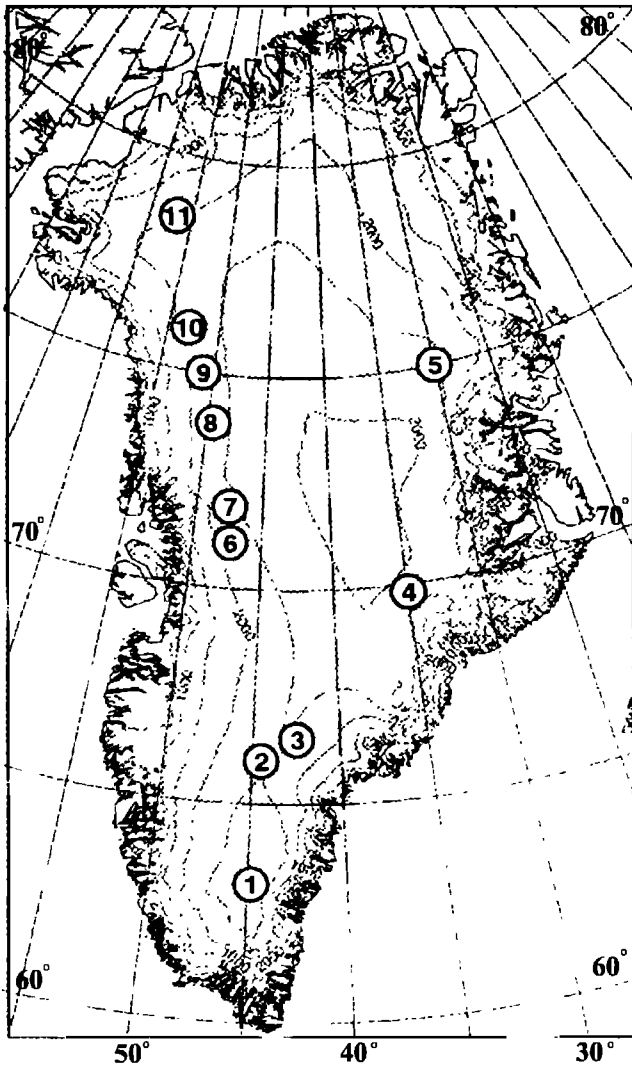


Figure 3. Elevation map of the Greenland ice sheet showing ice core locations near the 2000 m elevation contour from McConnell *et al.*, 2000a.

of the multiyear mean errors over all ice cores is defined by

$$\bar{\epsilon}_j = \frac{1}{J} \sum_{j=1}^J \epsilon_j. \quad (37)$$

The multiyear mean errors  $\epsilon_j$  at the site  $j$  of the modeled precipitation from various methods and their spatially averaged values  $\bar{\epsilon}_j$  over all ice cores are shown in Table 1. The spatial average of the multiyear mean error  $\bar{\epsilon}_j$  for the improved method is  $11.5 \text{ cm yr}^{-1}$ , while that for the  $P$  and  $P-E$  from ERA-15 is  $14.5$  and  $14.0 \text{ cm yr}^{-1}$ , respectively. Thus the spatial average of the multiyear mean error  $\bar{\epsilon}_j$  of the modeled precipitation computed from the improved method is smaller than that for  $P$  and  $P-E$  from ERA-15. However, the multiyear mean errors  $\epsilon_j$  from ERA-15 are smaller at some ice core sites.

The multiyear mean observed annual accumulation and modeled annual precipitation over the 9 years at site  $j$  are defined by

$$M_{obs,j} = \frac{1}{Y} \sum_{y=1}^Y (obs)_{y,j}, \quad M_{mod,j} = \frac{1}{Y} \sum_{y=1}^Y (mod)_{y,j}, \quad (38)$$

respectively, and their spatially averaged error over all ice cores is defined by

$$\epsilon_M = \frac{1}{J} \sqrt{\sum_{j=1}^J (M_{mod,j} - M_{obs,j})^2}, \quad (39)$$

and it is referred to as a total mean error. The total mean error describes the mean difference between the multiyear mean observed annual accumulation and modeled annual precipitation over all ice cores, and it determines the accuracy of the horizontal distribution of the modeled precipitation. The multiyear mean observed annual accumulation,  $M_{obs,j}$ , and modeled annual precipitation,  $M_{mod,j}$ , at the different site  $j$  and the total mean errors  $\epsilon_M$  for the different methods are given in Table 2. It is easily seen from Table 2 that the total mean error  $\epsilon_M$  for the improved methods is  $3.0 \text{ cm yr}^{-1}$ , while that  $\epsilon_M$  for the  $P$  and  $P-E$  from ERA is  $4.0$  and  $3.8 \text{ cm yr}^{-1}$ , respectively. These total mean errors show that the precipitation modeled by the improved method is better than the  $P$  and  $P-E$  of ERA-15 at these 11 sites. From Tables 1 and 2 we can conclude that the distribution of precipitation over the ice core sites retrieved by the improved dynamic method is considerably improved.

Site 4 is located at  $69.8^\circ\text{N}$ ,  $35.0^\circ\text{W}$ , and it is at the margin of a zone of very large precipitation gradient. A slight shift in the model simulation will easily give a different precipitation amount. If the model cannot simulate the mesoscale features, it is difficult to get a good precipitation result at this site. The mean value of the retrieved precipitation from the improved dynamic method at this site shown in Table 2 is  $23.1 \text{ cm yr}^{-1}$ , while the mean values of the  $P$  and  $P-E$  from ERA-15 in Table 2 are  $25.0$  and  $25.3 \text{ cm yr}^{-1}$ , respectively. However, the mean value of the measured time series of the accumulation at site 4 shown in Table 2 is  $48.2 \text{ cm yr}^{-1}$ , and it is about 2 times the simulated precipitation. This large error shows that the models must be developed further in order to capture the mesoscale features of the precipitation at this site.

#### 4. Trend of the Annual Precipitation Over Greenland in Recent Years

The temporal changes present in the precipitation time series produced by the improved dynamic method are here contrasted with those reported previously from the old dynamic method. We concentrate on the trend of annual precipitation over Greenland. It was reported by Bromwich *et al.* [1999] that the old dynamic method revealed a significant downward trend in annual precipitation from 1985 to 1995 for all of Greenland and its southern and central west coastal regions, amounting to 3% per year. Table 3 presents the linear trends in seasonal and annual retrieved precipitation from the improved dynamic method for all of Greenland and the individual sectors. The trends from the old and improved dynamic approaches are similar and the trend accelerates from 1995 to 1999 using the improved dynamic method.

The surface elevation change of the Greenland ice sheet is of considerable importance to the change of global sea level. The elevation of the ice sheet surface rises and falls over a

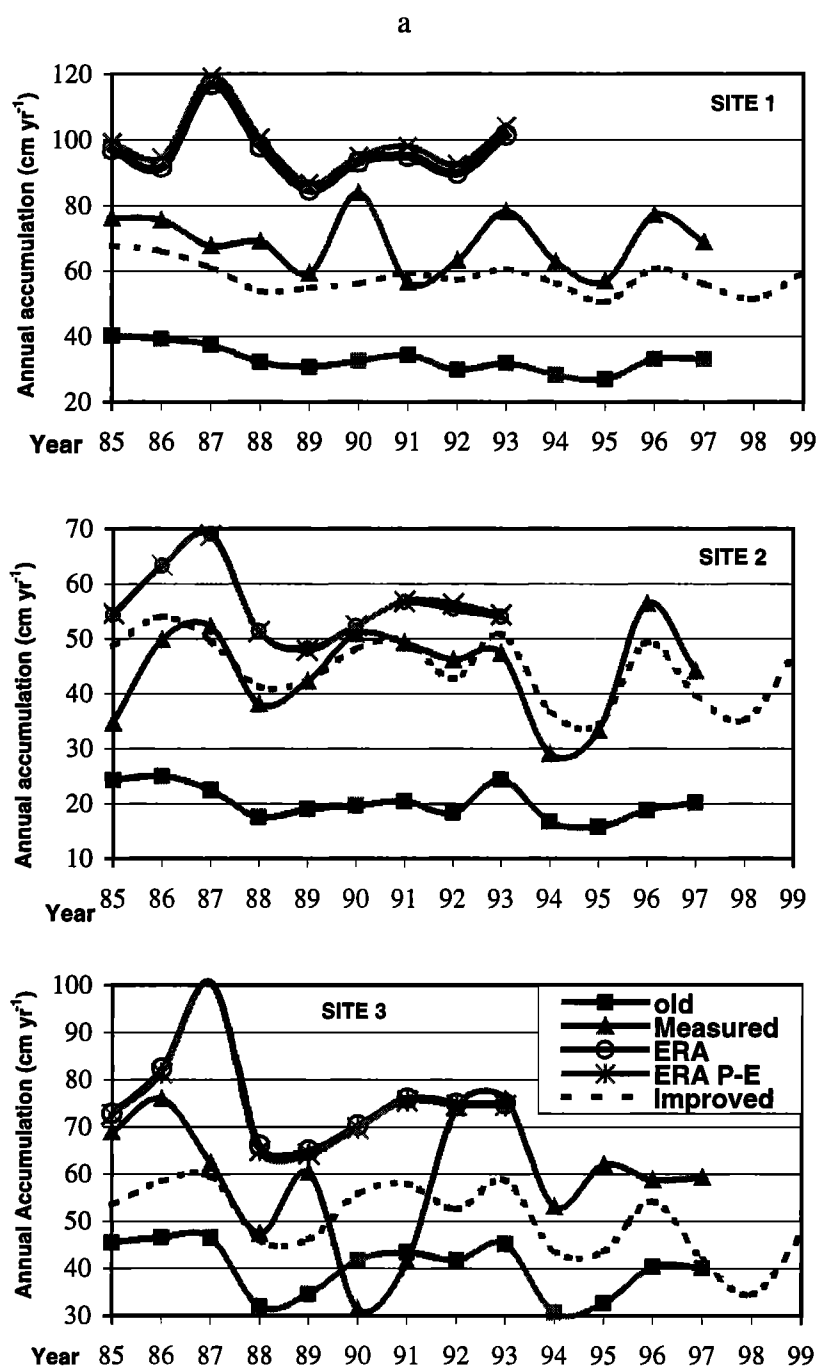


Figure 4. (a) Interannual variations of the measured accumulation and modeled precipitation from various methods at the ice core sites 1, 2 and 3; (b) same as Figure 4a but at the ice core sites 4, 5, and 6; (c) same as Figure 4a but at the ice core sites 7, 8, and 9; (d) same as Figure 4a but at the ice core sites 10 and 11. Here the "old" means the original method with the topography of Figure 1a.

relatively short period simply because of snow accumulation, firm densification, and snow melting rates. Snowmelt on the Greenland ice sheet derived from passive microwave satellite data was studied by *Abdalati and Steffen* [1995; 1997], and the melt is found to be most extensive on the western side of the ice sheet with a maximum in late July. Moreover, there is a notable increasing trend in melt area between the years 1979 and 1991 of 4.4% per year, which in general exceeds one standard deviation of the natural melt area variability. Recent

advances in airborne laser altimetry and global positioning system (GPS) technology have made possible large-scale assessment of elevation change characteristics of the entire ice sheet through repeated surveys separated in time. Such repeated surveys in 1993 and 1998 [*Krabill et al.*, 1999] showed that the southeast margin of the Greenland ice sheet has been thinning. *McConnell et al.* [2000b] derived changes in ice sheet elevation in southern Greenland, for the years 1978-1988, using a physically based model of firm

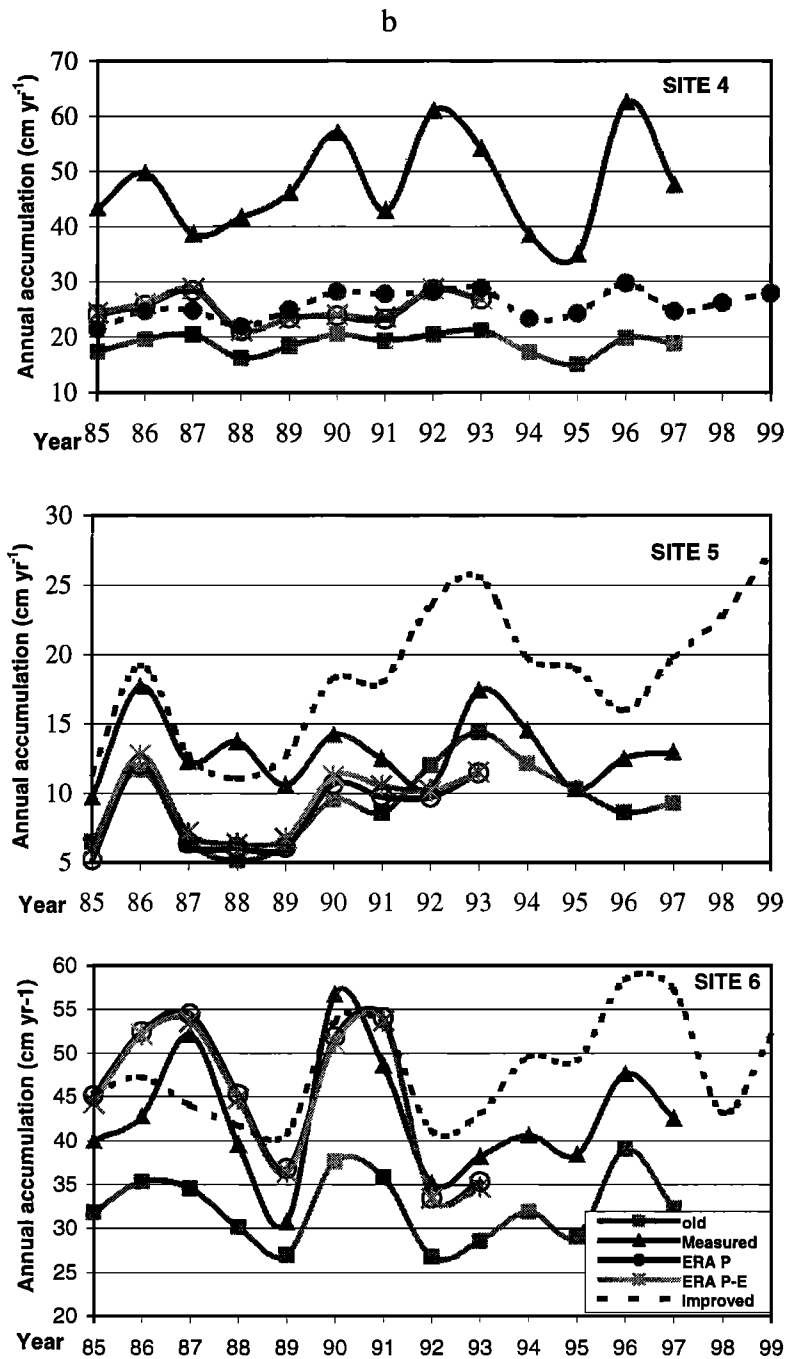


Figure 4. (continued)

densification and records of annual snow accumulation reconstructed from 12 ice cores at high elevation (above about 2000 m). They found that the patterns of elevation change derived from snow accumulation agree closely with contemporaneous satellite measurements of the surface elevation change of the ice sheet. The snow accumulation is a net result of precipitation, evaporation/sublimation, and drifting snow. To understand what is responsible for the changes of the surface elevation and snow accumulation over Greenland, it is necessary to investigate the corresponding change of precipitation.

The modeled precipitation needs to be validated by *in situ* measurements. Figure 5 shows the average normalized time

series of annual accumulation from ice core sites 1-3 in southern Greenland above 2000 m (Figure 3) along with the corresponding precipitation time series from the nearest grid point produced by the improved dynamic method. This compositing is done to represent the averaged results over the southern Greenland above 2000 m. On basis of the *Thomas et al.* [1999] studies, the general agreement between satellite radar altimeter (1978-1988) and airborne laser altimeter (1993-1998) results provides strong evidence that as a whole, the southern Greenland ice sheet above 2000 m has been in balance even if there are areas of thickening or thinning within the region. It is seen from Figure 5 that there is no obvious trend from the spatially smoothed precipitation and

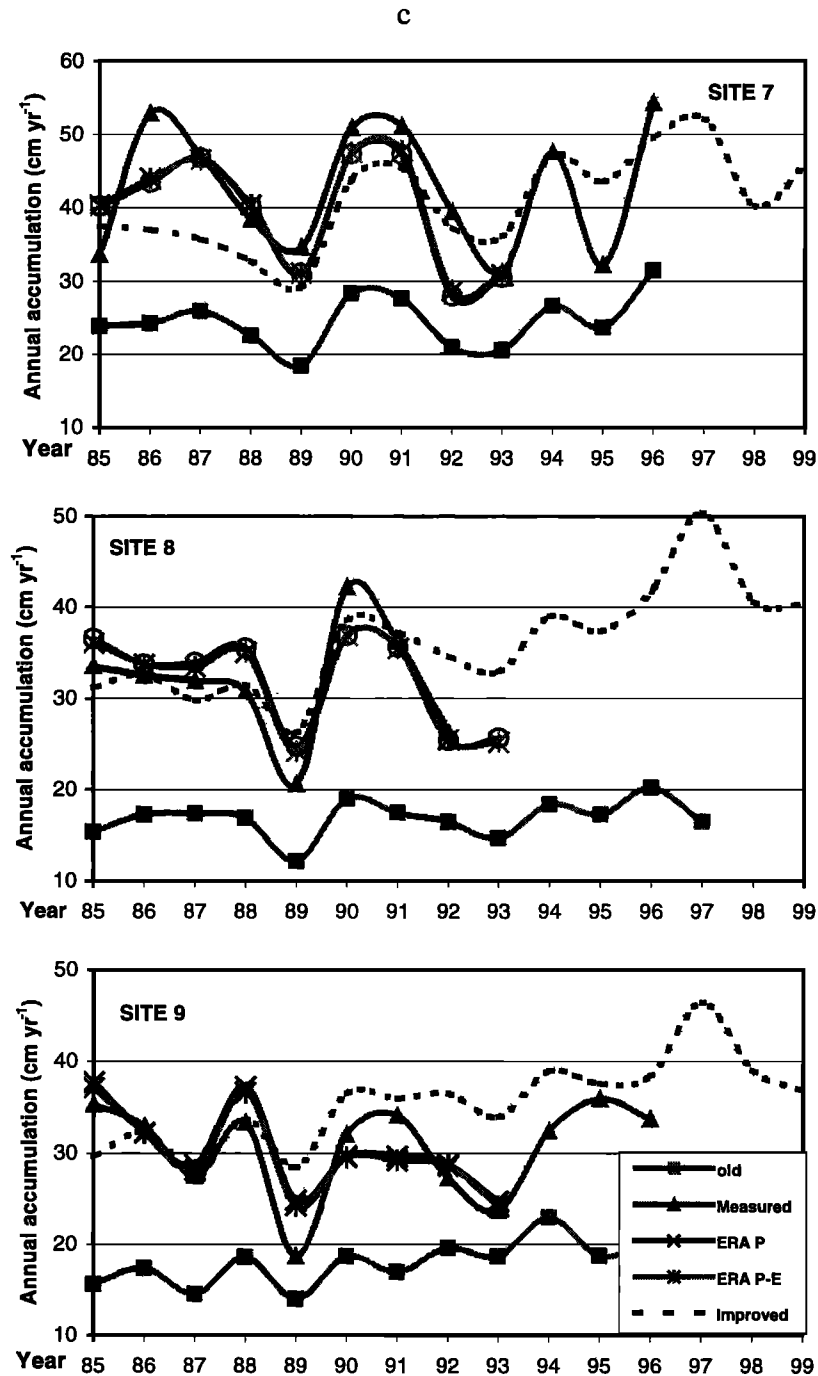


Figure 4. (continued)

accumulation averaged over many grid points of the southern Greenland above 2000 m and that most of the high, observed annual accumulation variability is reproduced by the model. The modeled precipitation from the improved dynamic method and observed accumulation from ice cores are in agreement with the *Thomas et al.* [1999] result that the southern Greenland Ice Sheet above 2000 m is approximately in balance.

Aircraft laser-altimeter surveys over northern Greenland in 1994 and 1999 have also been studied by *Krabill et al.* [2000], and they reported changes in the surface elevation of Greenland between 1993 and 1999 derived from radar and

laser altimetry and estimated coastal melting (Plate 1). It is found that above 2000 m elevation, the entire ice sheet is in balance on average but has some regions of local thickening or thinning. Below 2000 m surface elevation, thinning predominates along 70% of the coast, with rates about 1 m per year close to the coast. At the lower elevations below 1700 m, radar altimeter data become unreliable [*Thomas et al.*, 1999]. *Krabill et al.* [2000] calculated a hypothetical thinning rate at the coast on the basis of the coast positive degree day (PDD) anomalies, using a factor of 9 mm per PDD. From this approach, only melt is considered near the coast in the thinning rate.

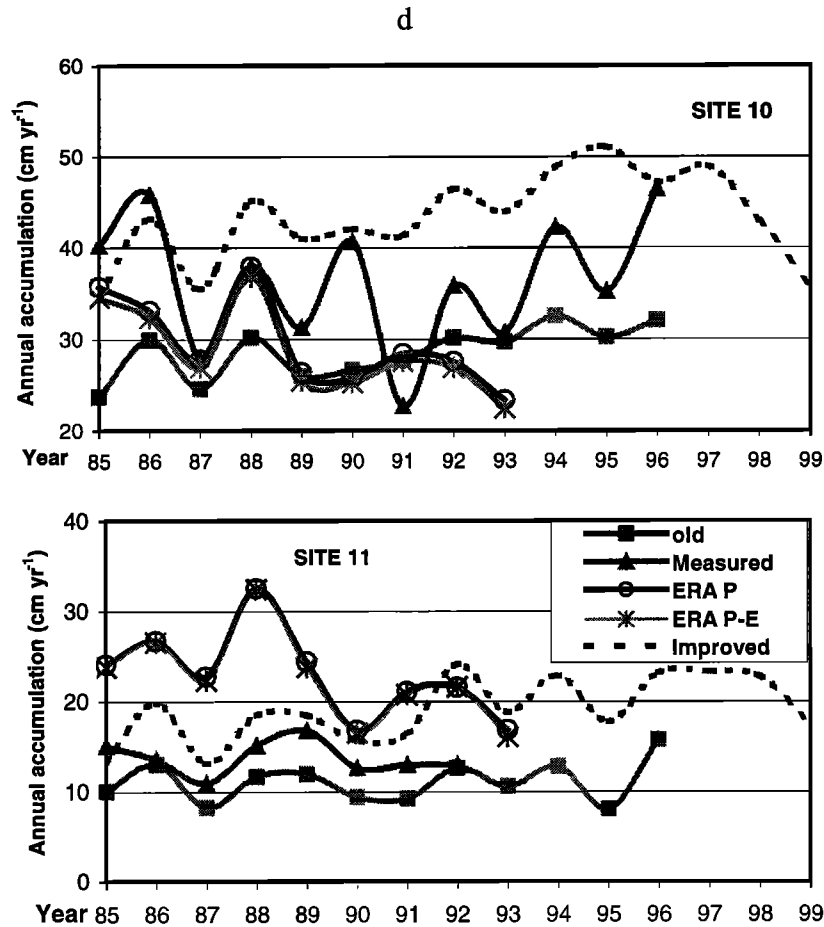


Figure 4. (continued)

Above 2000 m surface elevation, most of northern ice sheet lies above the region of summer melting. Because *McConnell et al.* [2000b] found that altimetry-derived estimates of ice sheet thickening and thinning from 1978 to 1988 over southern Greenland above 2000 m are consistent with elevation changes caused by temporal variability in snow accumulation, the effects of melting on the surface elevation

change of southern Greenland above 2000 m should also be small. Thus melting is very small over both northern and southern Greenland above 2000 m. To compare the temporal variability of precipitation with that of surface elevation over the entire Greenland above 2000 m, the spatial distribution of the slope of the linear regression line of the annual precipitation from the improved dynamic method for 1993-

Table 1. Yearly Mean Error  $\epsilon_j$ , of the Modeled Precipitation From Various Methods at Each Site(j) and the Mean Values,  $\epsilon_j$ , Averaged Over All Sites

Site	Old Method	Improved Method	P From ERA-15	P-E From ERA-15
1	36.66	13.22	31.11	28.70
2	25.11	5.40	11.83	11.94
3	22.75	16.24	22.65	22.21
4	29.71	23.36	24.17	23.97
5	4.97	5.81	4.96	4.46
6	11.66	5.88	5.37	5.15
7	19.44	7.95	5.85	5.56
8	15.47	4.37	3.06	2.85
9	13.30	6.14	3.15	2.93
10	9.88	9.85	8.02	8.54
11	3.32	5.17	10.14	9.90
Mean value	21.36	11.49	14.48	14.02

Table 2. Annual Mean Values of the Observed Accumulation,  $M_{obs,j}$ , and Various Modeled Precipitation,  $M_{mod,j}$ , at Site  $j$ , As Well As the Mean Error Over All Sites  $\epsilon_M$

Site	Observed	Old Method	Improved Method	P From ERA-15	P-E From ERA-15
1	69.98	34.28	53.75	98.97	96.45
2	45.60	21.21	42.73	56.10	56.23
3	59.72	41.88	48.84	75.92	75.30
4	48.24	19.25	23.05	25.02	25.26
5	13.17	8.95	15.25	8.60	9.19
6	42.63	31.95	41.00	45.41	44.91
7	42.13	23.58	33.48	39.39	39.68
8	31.72	16.28	29.43	31.98	31.72
9	29.42	17.12	29.48	30.38	29.95
10	34.79	27.62	37.31	29.57	28.70
11	13.78	10.76	15.85	22.99	22.66
Mean error		5.71	3.04	3.96	3.77

1999 has been computed, and it covers the same period as that of Plate 1. A color-coded figure of the slope of the linear regression line of the annual precipitation from 1993-1999 is shown in Plate 2. In northern Greenland (north of 70°N) above 2000 m, there are three thickening areas shown in Plate 1, and they are centered at about (74°N, 48°W), (76°N, 28°W) and (78°N, 52°W), respectively. Except for coastal regions, there is only one thinning area centered at about (76°N, 44°W) shown in Plate 1. These three thickening and one thinning regions, respectively, correspond to three positive and one negative areas of precipitation change centered at about the same locations in Plate 2. It should be pointed out that the unit used in Plate 2 is cm/year in water equivalent, and a multiplying factor of about 3.3 is necessary to transform the water equivalent values to the thickness of snow (R. Thomas, personal communication, 2001).

In southern Greenland above 2000 m, there is a major thinning area over its western part and south of 66°N, and there are also three thickening areas located at about (68°N, 38°W), (67°N, 47°W) and (63°N, 47°W) shown in both Plates 1 and 2, respectively. From the above, it is seen that altimetry-derived estimates of ice sheet thickening and thinning from 1993 to 1999 over the entire Greenland above 2000 m are approximately consistent with precipitation change retrieved by the improved dynamic method.

It is obvious that a positive precipitation increase region centered at about (70°N, 28°W) shown in Plate 2 is not matched to thickening in Plate 1. This area is near the coast where the melt is important [Abdalati and Steffen, 1997]. It is possible that the precipitation increase is greatly reduced by the melt in this region. Even if the precipitation trends are multiplied by 3.3 to get snow thickness changes, the magnitude of the computed snow thickness changes in the

region where the precipitation trend is positive is smaller than the observed changes in surface elevation. This may be due to deficiencies in the precipitation retrieval or other causes.

Krabill *et al.* [2000] excluded measured surface elevation change in coastal areas; instead, an interpolation was used between the calculated PDD thinning rates due to melting and nearest observed elevation changes to yield thinning rates over the ice-covered coastal regions. Change of surface elevation over the ice sheet is due to not only the effects of melting but also to those of firm densification and snow accumulation, in which precipitation predominates. It is not appropriate that only melting is considered in estimating the change of surface elevation of ice sheet even in the coastal areas. At least, the sum of precipitation and melting must be used. On the other hand, thinning rates exceeding 1 m/yr over the coastal areas are probably too large to be caused by these factors. We note that there are many precipitation decrease areas along the coast shown in Plate 2, especially in southern Greenland, and they likely contribute to the surface elevation thinning in the coastal regions. Thus it is appropriate to estimate thickening and thinning of surface elevation over coastal regions by using precipitation and melting together.

## 5. Conclusion and Discussions

On the basis of the evaluation of recent Greenland precipitation studies, several of the deficiencies in the modeled precipitation are probably related to the topographic data employed in assimilation and modeling. The topography of the Greenland ice sheet based on the U.S. Navy 10 arc min global data set and based on the modern data set synthesized from a variety of observations including satellite radar altimetry [Ekholm, 1996] are compared and shown in Figures 1a and 1b,

Table 3. Linear Change With Time ( $\pm 1$  S.D.) of the Retrieved Precipitation Amount from the Improved Dynamic Method (1985-1999) (cm/yr)

Region	DJF	MAM	JJA	SON	Annual
North	-0.35 $\pm$ 3.0	0.21 $\pm$ 2.8	-10.4 $\pm$ 6.2	4.2 $\pm$ 2.8	-1.5 $\pm$ 2.7
Central-west	-1.1 $\pm$ 5.4	1.2 $\pm$ 5.4	-13.7 $\pm$ 4.5	-5.6 $\pm$ 5.4	-4.7 $\pm$ 1.5
Central	1.4 $\pm$ 2.3	3.3 $\pm$ 1.4	3.1 $\pm$ 2.3	3.1 $\pm$ 2.1	2.8 $\pm$ 4.3
Central-east	4.8 $\pm$ 6.4	10.0 $\pm$ 4.5	-0.2 $\pm$ 6.8	7.7 $\pm$ 6.1	5.4 $\pm$ 4.3
South	-29.3 $\pm$ 12.4	-26.7 $\pm$ 8.4	-21.9 $\pm$ 6.7	-8.5 $\pm$ 10.5	-19.4 $\pm$ 4.4
Greenland	-8.3 $\pm$ 6.0	-6.0 $\pm$ 3.4	-10.0 $\pm$ 3.2	-2.6 $\pm$ 4.2	-6.5 $\pm$ 2.0

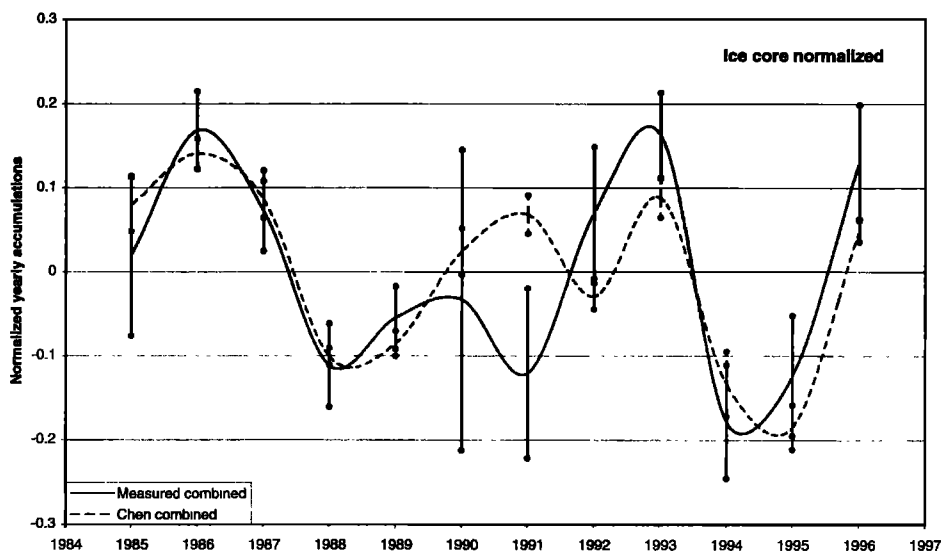


Figure 5. Normalized annual accumulation amounts (departures from the mean divided by the mean) and normalized annual precipitation amounts averaged for ice core sites 1-3 (see Figure 3). The standard errors of the mean are plotted as vertical bars.

respectively. If the horizontal pressure gradient force in  $\sigma$  coordinates is separated into its irrotational and rotational parts, which are expressed by the equivalent geopotential and geo-stream-function, respectively (CB99), the topographic effect on the precipitation can be more accurately modeled than the original expression (2). The equivalent geopotential and geo-stream-function are implemented in a more consistent manner in this paper than the original dynamic method [Chen *et al.*, 1997a; CB99, Bromwich *et al.*, 1999]; the term  $\Phi_{e,had,i} \downarrow$  in the generalized  $\omega$ -equation is expressed by (26) instead of (6.19) of CB99. A simplified large-scale condensation without condensate evaporation is also used. These procedures are combined with the corrected topography of Figure 1b, and the new method is referred to as the improved dynamic method.

The precipitation distribution retrieved by the improved dynamic method and shown in Figure 2b is better than that captured by the original method and shown in Figure 2a. The  $10 \text{ cm yr}^{-1}$  contour near Summit, Greenland, in Figure 2b is much closer to that of the measured accumulation (Figure 2c) than that in Figure 2a. A relatively large precipitation area centered near the point ( $70^\circ\text{N}$ ,  $49^\circ\text{W}$ ) is present in Figure 2b but absent from Figure 2a.

McConnell *et al.* [2000a] showed that the modeled precipitation from the original method with the topography of Figure 1a must use scalars to have a high degree of correspondence in the interannual variations between the measured accumulation and the retrieved precipitation. However, the retrieved precipitation from the improved method increases at all of the ice core sites, and a good correspondence in the interannual variations between the measured accumulation and the retrieved precipitation is obtained without the use of any scalar.

The average value  $\bar{\epsilon}_j$  over all ice cores of the annual mean error at each of  $j$  sites for the improved method is  $11.5 \text{ cm yr}^{-1}$ , while that for the  $P$  and  $P-E$  from ERA-15 is  $14.5$  and  $14.0 \text{ cm yr}^{-1}$ , respectively. The mean error over all ice cores of

the annual mean value at each site  $j$ ,  $\epsilon_M$ , for the improved method is  $3.0 \text{ cm yr}^{-1}$ , while  $\epsilon_M$  for the  $P$  and  $P-E$  from ERA-15 is  $4.0$  and  $3.8 \text{ cm yr}^{-1}$ , respectively. Both errors show that the precipitation modeled from the improved method is better than the  $P$  and  $P-E$  from ERA-15. Thus the distribution of precipitation retrieved by the improved dynamic method over the 11 ice core sites is considerably improved.

Large downward trends in annual amounts are present in the precipitation retrieved by the improved dynamic method for all of Greenland and its southern and central west coastal regions. The trends from the old and improved dynamic approaches are similar and the trend accelerates from 1995 to 1999 using the improved dynamic method. The modeled precipitation from the improved dynamic method and observed accumulation from ice cores are all in agreement with the Thomas *et al.* [1999] result that the southern Greenland ice sheet above 2000 m is approximately in balance. It is also seen that altimetry-derived estimates of ice-sheet thickening and thinning from 1993 to 1999 over the entire Greenland above 2000 m are approximately consistent with the precipitation change retrieved by the improved dynamic method.

However, it is seen in section 3 that there are at least three remaining deficiencies in the retrieved precipitation. One is that the relatively large accumulation with the contour value of  $50 \text{ cm yr}^{-1}$  in the region centered near the point ( $70^\circ\text{N}$ ,  $47^\circ\text{W}$ ) shown in Figure 2c is not well simulated by the improved method. The second is that the annual mean errors  $\epsilon_j$  of the precipitation modeled by the improved method are pretty large at some sites, and the average value over all ice cores  $\bar{\epsilon}_j$  ( $11.5 \text{ cm yr}^{-1}$ ) is still very large. The third, which might be more fundamental, is that some mesoscale features of the Greenland precipitation are not well simulated. These three deficiencies need to be corrected.

It has been mentioned in section 1 that the time scale of accumulation of ice core sites is several years, but its horizontal variation scale is kilometers. Both precipitation

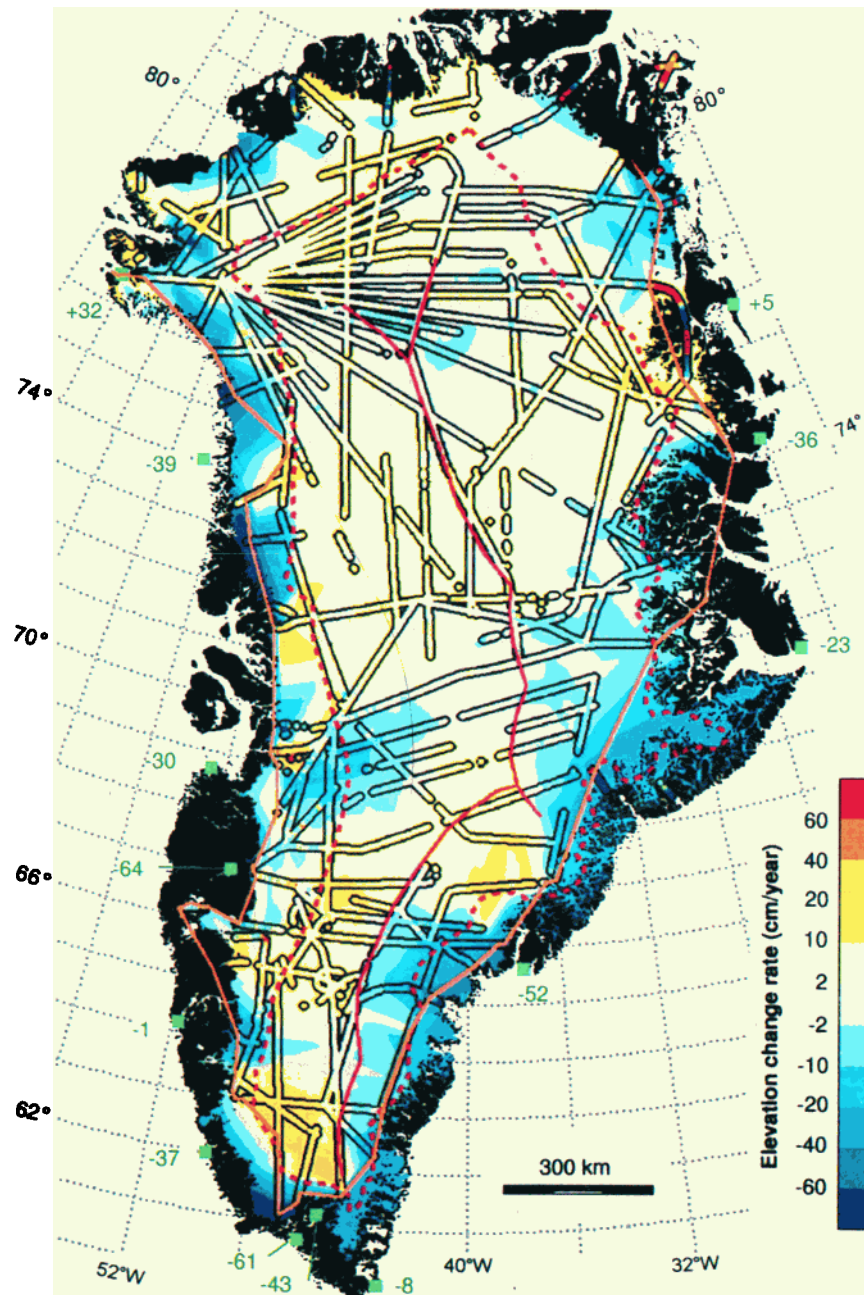


Plate 1. Greenland ice-surface elevation change  $dh/dt$  (in unit cm/year) for 1993-1999 derived mostly from airborne laser-altimetry (colors with scale at bottom right). The black hollow lines show the flight tracks. Pale gray segments are in balance within the survey errors ( $\pm 2$  cm/yr). In the area near the coast (outside the pink boundary), surface elevation change is interpolated between flight-track data and hypothetical values from melt at coastal weather stations. The 13 coastal stations are shown in green along with the  $dh/dt$  value derived from the PDD anomalies. The violet solid and dashed lines are major ice-sheet ridges and the 2000-m elevation contour, respectively. Reprinted with permission from *Krabill et al.* [*Science*, 289, 482, 2000]. Copyright [2000] American Association for the Advancement of Science.

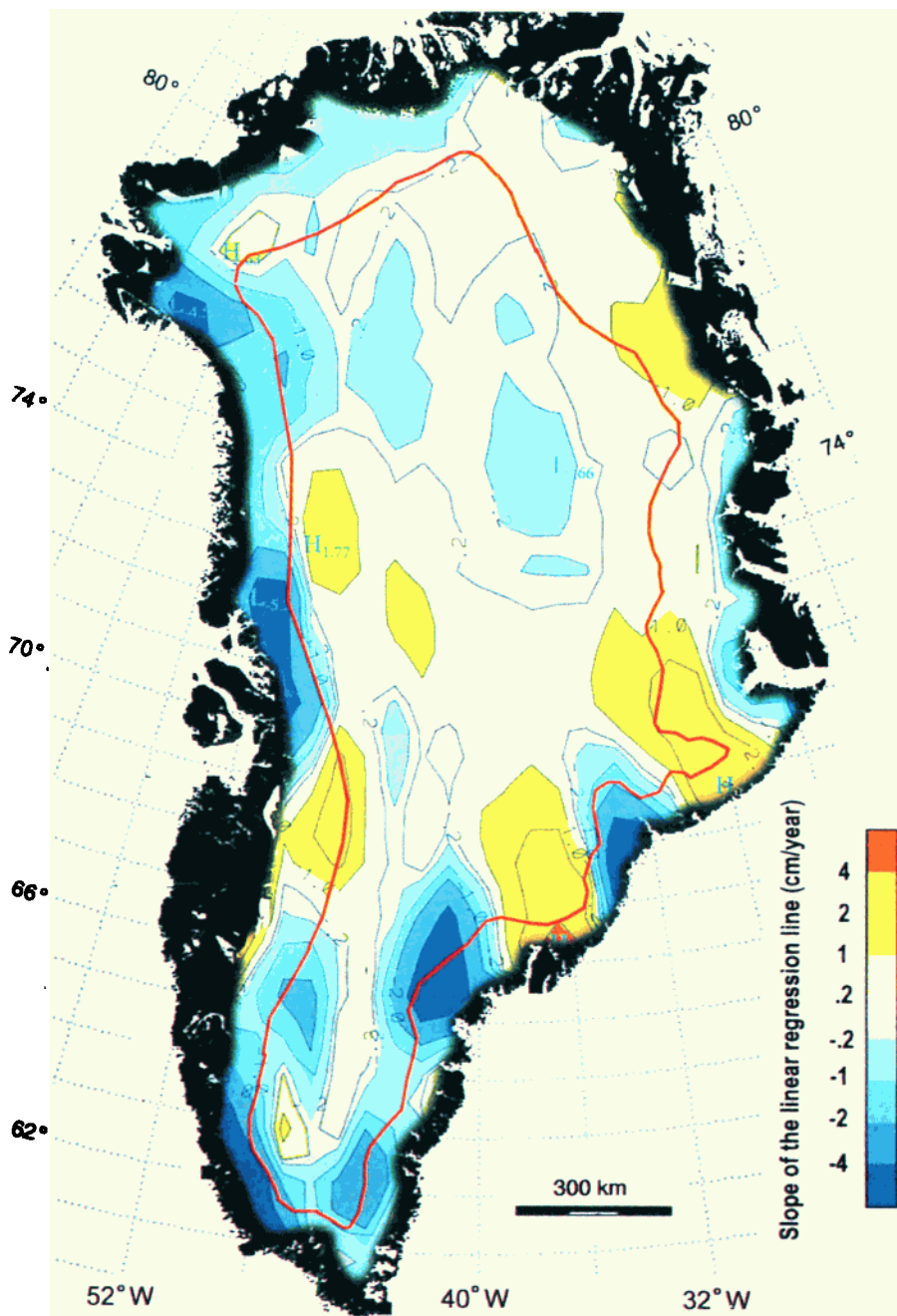


Plate 2. Distribution of the annual precipitation trend over Greenland except for the coastal region (elevation below 1000 m) in unit cm/yr (in water equivalent, multiply by 3.3 to get snow thickness changes) for 1993-1999 derived from the improved dynamic method (colors with scale at bottom right). The red solid line is the 2000 m elevation contour.

computed by the improved dynamic method for 1985-1999 and that computed from the original method with the topography of Figure 1a for 1985-1995 all use a 50 km grid length. The computed results in section 3 show that the mesoscale features of the distribution of the annual mean precipitation over Greenland need further improvement.

**Acknowledgments.** This research was sponsored by NASA grants NAG5-6001 and NAG5-016001 to the first author. ECMWF operational analysis data were obtained from NCAR via grant 3706880. We thank the three anonymous reviewers for their many positive comments. This is contribution 1224 of Byrd Polar Research Center.

## References

- Abdalati, W., and K. Steffen, Passive microwave-derived snowmelt regions on the Greenland ice sheet, *Geophys. Res. Letts.*, **22**, 787-790, 1995.
- Abdalati, W., and K. Steffen, Snowmelt on the Greenland ice sheet as derived from passive microwave satellite data, *J. Clim.*, **10**, 165-175, 1997.
- Anthes, R. A., Recent applications of the Penn State/NCAR mesoscale model to synoptic, mesoscale, and climate studies, *Bull. Am. Meteorol. Soc.*, **71**, 1610-1629, 1990.
- Bromwich D. H., F. M. Robasky, R. A. Keen, and J. F. Bolzan, Modeled variations of precipitation over the Greenland ice sheet, *J. Clim.*, **6**, 1253-1268, 1993.
- Bromwich D. H., R. I. Cullather, Q.-S. Chen, and B. M. Csatho, Evaluation of recent precipitation studies for the Greenland ice sheet, *J. Geophys. Res.*, **103**, 26,007-26,024, 1998.
- Bromwich, D. H., Q.-S. Chen, Y. Li, and R. I. Cullather, Precipitation over Greenland and its relation to the North Atlantic Oscillation, *J. Geophys. Res.*, **104**, 22,103-22,115, 1999.
- Cassano, J. J., J. E. Box, D. H. Bromwich, L. Li, and K. Steffen, Evaluation of Polar MM5 simulations of the Greenland atmospheric circulation, *J. Geophys. Res.*, this issue.
- Chen, Q.-S., and D. H. Bromwich, An equivalent isobaric geopotential height and its application to synoptic analysis and to a generalized  $\omega$ -equation in  $\sigma$  coordinates, *Mon. Weather Rev.*, **127**, 145-172, 1999.
- Chen, Q.-S., and Y.-H. Kuo, A harmonic-sine series expansion and its application to the partitioning and reconstruction problem in a limited area, *Mon. Weather Rev.*, **120**, 91-112, 1992.
- Chen, Q.-S., Y.-H. Kuo, and D. H. Bromwich, A balanced ageostrophic initialization with a fixed external wind boundary value for limited-area models, *J. Meteorol. Soc. Jpn.*, **74**, 325-342, 1996.
- Chen, Q.-S., D. H. Bromwich, and L. Bai, Precipitation over Greenland retrieved by a dynamic method and its relation to cyclonic activity, *J. Clim.*, **10**, 839-870, 1997a.
- Chen, Q.-S., L. Bai, and D. H. Bromwich, A harmonic-Fourier spectral limited-area model with an external wind lateral boundary condition, *Mon. Weather Rev.*, **125**, 143-167, 1997b.
- Colle B. A., K. J. Westrick, and C. F. Mass, Evaluation of MM5 and Eta-10 precipitation forecasts over the Pacific Northwest during the cool season, *Weather Forecasting*, **14**, 137-154, 1999.
- Csatho, B., H. Xu, R. Thomas, D. H. Bromwich, and Q.-S. Chen, Comparison of accumulation and precipitation maps of the Greenland Ice Sheet, *EOS. Trans. AGU*, **78(46)**, Fall. Meet. Suppl., F9, 1997.
- Ekhholm, S., A full coverage, high-resolution, topographic model of Greenland computed from a variety of digital elevation data, *J. Geophys. Res.*, **101**, 21,961-21,972, 1996.
- Genthon, C., and A. Braun, ECMWF analyses and predictions of the surface climate of Greenland and Antarctica, *J. Clim.*, **8**, 2324-2332, 1995.
- Gibson J. K., P. Kallberg, S. Uppala, A. Hernandez, A. Nomura, and E. Serrano, ERA description, in *ECMWF Re-Analysis Project Report series vol. 1*, 72 pp., Eur. Cent. for Medium-Range Weather Forecasts, Reading, UK, 1997.
- Haltiner, G. J., and R. T. Williams., *Numerical Prediction and Dynamical Meteorology*, 477 pp., John Wiley & Sons, New York, 1980.
- Kalnay, E., et al., The NCEP/NCAR 40-year reanalysis project, *Bull. Am. Meteorol. Soc.*, **77**, 437-471, 1996.
- Krabill, W., E. Frederick, S. Manizade, C. Martin, J. Sonntag, R. Swift, R. Thomas, W. Wright, and J. Yungel, Rapid thinning of parts of the southern Greenland ice sheet, *Science*, **283**, 1522-1524, 1999.
- Krabill, W., W. Abdalati, E. Frederick, S. Manizade, C. Martin, J. Sonntag, R. Swift, R. Thomas, W. Wright, and J. Yungel, Greenland ice sheet: High-elevation balance and peripheral thinning, *Science*, **289**, 428-430, 2000.
- McConnell, J. R., E. Mosley-Thompson, D. H. Bromwich, R. C. Bales, and J. F. Kyne, Interannual variations of snow accumulation on the Greenland ice sheet (1985-1996): New observations versus model predictions, *J. Geophys. Res.*, **105**, 4039-4046, 2000a.
- McConnell, J. R., R. J. Arthern, E. Mosley-Thompson, C. N. Davis, R. C. Bales, R. Thomas, J. F. Burkhart, and J. F. Kyne, Changes in Greenland ice sheet elevation attributed primarily to snow accumulation variability, *Nature*, **406**, 877-879, 2000b.
- Pauley, P. M., and S. J. Nieman, A comparison of quasi-geostrophic and non-quasigeostrophic vertical motions for a rapidly intensifying marine extratropical cyclone, *Mon. Weather Rev.*, **120**, 1108-1134, 1992.
- Thomas, R., C. Davis, E. Frederick, S. Manizade, J. Sonntag, W. Krabill, and J. McConnell, Greenland ice sheet elevation change since 1978 from radar and laser altimetry, *Polar Geogr.*, **23**, 169-184, 1999.

D. H. Bromwich, L. S. Bai, Q. S. Chen, and Y. Li, Polar Meteorology Group, Byrd Polar Research Center, 1090 Carmack Rd., The Ohio State University, Columbus, OH 43210, USA. (bromwich.l@osu.edu)

E. N. Cassano, CIRES, University of Colorado, Boulder, CO 80309, USA.

(Received August 28, 2000; revised June 18, 2001; accepted June 26, 2001.)